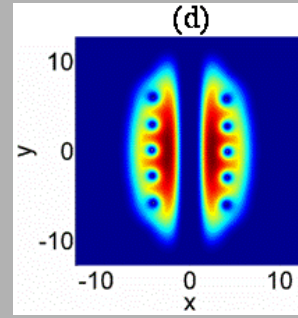


Abstract: We investigate the dynamics of vortex formation and the structure of vortex lattices in a Bose-Einstein condensate confined within a rotating double-well (DW) potential. The dynamical process is a formation process of “ghost” vortices, “hidden” vortices and “visible” vortices. The critical rotation frequency for the creation of visible vortex is indicated by a sudden jump in the angular momentum evolution and an inflexion in the energy evolution. Different visible vortex structures can be formed by ruling the rotation frequency. In particular, structural change of visible vortex patterns can be achieved by regulating the anisotropy parameter of the DW potential. This feature allows to flexibly control the distribution of angular momentum in macroscopic quantum systems and study the interplay among rotation, interparticle interaction and external potential in superfluids.



Linear visible vortex lattice pair in a Bose-Einstein condensate trapped in a rotating double-well potential

© by ASTRO, Ltd.
Published exclusively by WILEY-VCH Verlag GmbH & Co. KGaA

Formation and structure of vortex lattices in a rotating double-well Bose-Einstein condensate

L.H. Wen^{1*} and X.B. Luo²

¹ School of Physical Sciences and Information Engineering, Liaocheng University, Liaocheng 252059, China

² Department of Physics, Jinggangshan University, Ji'an 343009, China

Key words: Bose-Einstein condensate; vortex; double well; dynamics; structural change

PACS: 03.75.Lm, 03.75.Kk, 67.85.De

1. Introduction

Topological defects have been explored extensively in many systems, such as superfluids ^4He [1] and ^3He [2], superconductors [3], and cosmology [4]. Recently, increasing interest has been focused on the topological defects in ultra-cold atomic gases [5, 6, 7]. As an important example of topological defect, quantized vortex plays a fundamental role in the studies of atomic gases, ranging from manifesting superfluidity [8], collective excitations, long-range phase coherence [9], and universal phase transition dynamics of Bose-Einstein condensates (BECs) and degenerate Fermi gases [10]. In particular, for the vortices in dilute BECs, the theoretical description can be carried out in a much more efficient way than that in liquid He due to the low density and weak interatomic interaction.

To generate vortices in trapped BECs, different approaches, such as stirring a BEC with a laser [11, 12], phase imprinting, rotating traps [13], and vector gauge potential, have been used. Here we concentrate on the case

of rotating traps or equivalently rotating BECs. It is well known that for a BEC in a rotating harmonic trap there is a critical rotation frequency beyond which vortex starts to exist [6]. With the increasing of rotation frequency, more and more vortices appear. Structure of vortices depends on external trap potential. The vortices form a triangular lattice in a symmetry harmonic trap, i.e., the celebrated Abrikosov lattice [12]. While for rotating anisotropic harmonic traps [14, 15, 16] or atomic waveguides [17], linear vortex lattices [18], zigzag arrangements [19] and stripe-shaped configurations [20, 21, 22] might be generated. Furthermore, the vortex patterns undergo structural changes depending on the anisotropic parameter. Square vortex lattices and structural phase transitions (from triangular lattices to square lattices) has also been investigated in the system consisting of harmonic trap and optical lattice [23]. Meanwhile, the combined harmonic and quartic traps support giant vortices [24]. The toroidal traps can hold persistent flows with high winding numbers [25].

* Corresponding author: e-mail: linghuawen@126.com

To the best of our knowledge, most of the existing theories in the literature mentioned above directly use an imaginary time propagation (ITP) method or a lowest Landau level (LLL) approximation or a variational approach to study the properties of a rotating BEC. These methods are incapable of revealing the dynamics of vortex formation although they can be applied to find the steady states of a rotating system. In addition, these approaches can not deal with the BECs with dissipation that is universal and inevitable in real cold-atom experiments. Recently, a phenomenological dissipation model has been presented to study the dynamics of vortex formation of a BEC in a rotating harmonic trap, where elusive “ghost” vortices were revealed [26]. In a most recent investigation [27], the authors proposed an improved phenomenological dissipation model to test the well-known Feynman rule [6,28] of vortices in a rotating double-well (DW) BEC. It is found that there are three fundamental types of vortices in a rotating DW BEC: “visible” vortex, “ghost” vortex and “hidden” vortex. Only after including the hidden vortices can the Feynman rule be satisfied.

In this Letter, we study the dynamics of vortex formation in a BEC trapped in a rotating DW potential by using an improved phenomenological dissipation model [27]. The DW potential is particularly important due to its simplicity, universality and yet richness [29,30,31]. Meanwhile, it is a natural and flexible anisotropic trap. We discuss the structural change of visible vortex patterns in a rotating DW BEC by regulating the rotation frequency and the DW configuration. We find that the dynamical process of vortex formation in a rotating DW potential is remarkably different from that in a rotating harmonic trap [26]. The former case is a formation process of ghost vortices, hidden vortices and visible vortices. The critical rotation frequency for the generation of visible vortices is signaled by a sudden jump in the evolution of the average angular momentum per atom and an inflexion in the evolution of the average energy per atom. It is shown that the rotating drive excites a complex turbulent oscillation mainly consisting of the surface mode with $l = 4$ rather than the usual quadrupole oscillation consisting of quadrupole mode with $l = 2$ in the case of rotating harmonic trap [26]. Due to the parity effect, the vortex patterns of the rotating DW BEC in an equilibrium state display well centrosymmetry. By controlling the rotation frequency and the anisotropic parameter of the DW potential, the visible vortex pattern undergoes structural changes, including the formation of linear and zigzag vortex lattice pairs. In particular, the linear visible vortex lattice pairs have potential applications in quantum information processing due to the advantages of energetic stability, long-time coherence, controllable interaction and the least number of nearest neighbors.

2. Phenomenological dissipation model

By assuming strong confinement in the z direction, we consider a two-dimensional (2D) BEC trapped in a DW

potential

$$U(x, y) = \frac{m}{2}(\omega_x^2 x^2 + \omega_y^2 y^2) + U_0 e^{-x^2/2\delta^2}, \quad (1)$$

where m is the atomic mass, ω_x and ω_y are the angular frequencies of the harmonic trap in x and y directions, respectively. We introduce an anisotropy parameter $\lambda = \omega_y/\omega_x$ to describe the ratio between ω_y and ω_x . U_0 and δ denote the height and width of the potential barrier, respectively. The DW potential is allowed to rotate around the z axis with angular frequency Ω . In the rotating frame, the energy functional of the system becomes

$$\begin{aligned} E[\Psi, \Psi^*] &= \iint dxdy \left[\frac{\hbar^2 |\nabla \Psi|^2}{2m} + U(x, y) |\Psi|^2 - \Psi^* (\Omega L_z) \Psi \right] \\ &+ \frac{g_{2D}}{2} \iint dxdy |\Psi|^4, \end{aligned} \quad (2)$$

where $\Psi(x, y, t)$ is the wave function of the BEC, and $L_z = i\hbar(y\frac{\partial}{\partial x} - x\frac{\partial}{\partial y})$ denotes the z component of the angular-momentum operator. $g_{2D} = 2\sqrt{2\pi}\hbar^2 a_s/(a_z m)$ is the 2D interatomic interaction strength with a_s being the s -wave scattering length and $a_z = \sqrt{\hbar/(m\omega_z)}$ the axial harmonic length. If the dissipation of the BEC due to thermal clouds and rotation are ignored, one can obtain the time-dependent Gross-Pitaevskii (GP) equation in the rotating frame by using a variational method as follow

$$i\hbar \frac{\partial \Psi}{\partial t} = \left[-\frac{\hbar^2}{2m} (\nabla_x^2 + \nabla_y^2) + U(x, y) - \Omega L_z \right] \Psi + g_{2D} |\Psi|^2 \Psi. \quad (3)$$

The wave function is normalized as $N = \iint |\Psi|^2 dxdy$ with N being atom number. The stationary solutions $\Psi(x, y, t) = \Phi(x, y)e^{-i\mu t/\hbar}$ satisfy the time-independent GP equation

$$\begin{aligned} \mu \Phi &= \left[-\frac{\hbar^2}{2m} (\nabla_x^2 + \nabla_y^2) + U(x, y) - \Omega L_z \right] \Phi \\ &+ g_{2D} |\Phi|^2 \Phi, \end{aligned} \quad (4)$$

where μ is chemical potential.

Equation (4) or the imaginary time propagation of the time-dependent version (3) are widely used to study the properties of the stationary states of a rotating BEC. However, Eq. (3) and Eq. (4) can not reveal the dynamical process of the vortex formation. In Ref. [32], the authors numerically solved the time-dependent GP equation in a rotating frame, but the motion of created vortices remains turbulent and no vortex lattice forms. Moreover, Eq. (3) and Eq. (4) can not describe a BEC with dissipation.

Here we use a phenomenological dissipation model [27] to study the dynamics of vortex generation and the structure of the equilibrium state of rotating DW BEC. In this phenomenological model, the wave function $\Psi(x, y, t)$

obeys the following modified GP equation

$$(i - \gamma) \hbar \frac{\partial \Psi}{\partial t} = \left[-\frac{\hbar^2}{2m} (\nabla_x^2 + \nabla_y^2) + U(x, y) - \Omega L_z \right] \Psi + g_{2D} |\Psi|^2 \Psi, \quad (5)$$

where γ describes the degree of dissipation of the BEC. This model is a variation of that in Ref. [26] and has good predictive power. Our computation results for the case of a BEC in rotating harmonic trap are well in agreement with the experimental observations in Ref. [11] and the numerical results in Ref. [26]. Recently several other phenomenological models have also been proposed to deal with the BECs with dissipation [33, 34, 35, 36]. To numerically simulate Eq. (5), it is convenient to introduce dimensionless parameters as following $d_0 = \sqrt{\hbar/2m\omega_x}$, $\tilde{x} = x/d_0$, $\tilde{y} = y/d_0$, $\sigma = \delta/d_0$, $\tilde{t} = t\omega_x$, $V = U/\hbar\omega_x$, $V_0 = U_0/\hbar\omega_x$, $\tilde{\Omega} = \Omega/\omega_x$, $\tilde{L}_z = L_z/\hbar$ and $\psi = \Psi d_0/\sqrt{N}$. Thus Eq. (5) is reduced to a dimensionless form as

$$(i - \gamma) \frac{\partial \psi}{\partial t} = \left[-\left(\frac{\partial^2}{\partial x^2} + \frac{\partial^2}{\partial y^2} \right) + V(x, y) - \Omega L_z \right] \psi + c |\psi|^2 \psi, \quad (6)$$

where $c = g_{2D}N/(\hbar\omega_x d_0^2)$ denotes the dimensionless nonlinear strength and the tilde is omitted for simplicity. The rescaled 2D DW potential is expressed by

$$V(x, y) = \frac{1}{4}(x^2 + \lambda^2 y^2) + V_0 e^{-x^2/2\sigma^2}. \quad (7)$$

We numerically solve Eq. (6) with the split-step Fourier method [37, 38]. The initial quantum state $\psi(x, y, t = 0)$ in the DW potential can be obtained by the ITP method [39, 40, 41] for $\Omega = 0$. In our numerical computations, we use ^{87}Rb atoms and the parameters are chosen as $\omega_x = \omega_y = 2\pi \times 40$ Hz, $\omega_z = 2\pi \times 800$ Hz, $V_0 = 40$ and $\sigma = 0.5$. Here we take $\gamma = 0.03$, which corresponds to a temperature of around $0.1T_c$ [33]. In fact, the variation of the nonzero γ in Eq. (6) only influences the relaxation time scale but does not change the dynamics of the vortex formation and the ultimate steady structure of the system.

3. Dynamics of vortex formation

To reveal the dynamics of vortex formation in the rotating DW BEC for a fixed Ω , we show the time evolution of the density distribution $|\psi|^2$ and that of the corresponding phase distribution of $\psi(x, y, t)$ in Fig. 1 and Fig. 2, respectively. In Fig. 2, the value of the phase varies continuously from 0 to 2π , and the end point of the boundary between a 2π phase line and a 0 phase line corresponds to a phase defect (i.e., a vortex). Initially, the condensate density $|\psi(x, y, t = 0)|^2$ in a stationary DW potential is displayed in Fig. 1(a), and there is a zero relative phase between the two halves of the BEC as shown in Fig. 2(a).

With the development of time, the BEC undergoes complex turbulent oscillation [see Fig. 1(b)] instead of the usual elliptic oscillation in the case of rotating harmonic trap [26]. In Ref. [26], the elliptic oscillation is mainly caused by the quadrupole mode with angular momentum $l = 2$. Since the DW system has even parity with respect to the spatial coordinate, no surface modes with odd l are excited. Here the turbulent oscillation principally consists of the surface mode with $l = 4$ coupling with higher-energy modes through the nonlinear interaction, which is verified by the critical rotation frequency for visible vortex generation. The turbulent oscillation makes the boundary surfaces of the BEC unstable and excites the surface waves that propagate along the surfaces. Essentially, the surface ripples are resulted from the dynamical instability [42] associated with the imaginary frequency of the excitation modes. Then the surface waves develop into the vortex cores and most of the phase defects appear at the boundary surfaces of the cloud as shown in Fig. 2(b). Since the amplitude $|\psi|$ on the outskirts of the BEC is almost negligible, these phase defects can not be seen in the density distribution of Fig. 1(b) and neither carry angular momentum nor energy, they are called ghost vortices [26, 27].

At the same time, there are some phase singularities congregating and distributing symmetrically along the central barrier [see Figs. 2(b)-2(c)]. These phase singularities are known as the hidden vortices [27] because they carry evident angular momentum despite being invisible in the density distributions of Figs. 1(b)-1(c). With the further time evolution some ghost vortices penetrate into the BEC via the Landau instability [43] associated with the negative excitation frequency and becomes the usual visible vortices as shown in Figs. 1(d)-1(e) and Figs. 2(d)-2(e). In the presence of dissipation, a steady triangular lattice pair of visible vortices [see Fig. 1(f)] forms eventually due to the competition between the rotating drive propelling vortices toward the rotation axis and the repulsive interaction tending to push the vortices apart, where the energy of the system reaches the minimum in the rotating frame. The visible vortex density is determined by the parameters Ω , λ , V_0 , σ and c . As displayed in Fig. 2(f), most of the ghost vortices are repelled to the outside of the cloud. Since the DW potential is even parity concerning to the spatial coordinate, all the numbers of the visible vortices, hidden vortices and ghost vortices should be even, which can be seen clearly in Fig. 1(f) and Fig. 2(f). Physically, since vortex is a topological singularity, the system undergoes the change of topological property between the BEC with vortices and that without vortices when the external rotating drive inputs angular momentum into the BEC. Therefore the vortices are easier generated in the area of the lower density, such as the barrier boundary and the outskirts of the cloud [see Figs. 1(b)-1(c) and Figs. 2(b)-2(c)]. This is the reason why the hidden vortices and ghost vortices always appear before the visible vortices.

In Figs. 3(a)-3(b), we display the time evolution of the average angular momentum per atom $l_z = \iint \psi^* L_z \psi dx dy$ and the average energy per atom $\varepsilon =$

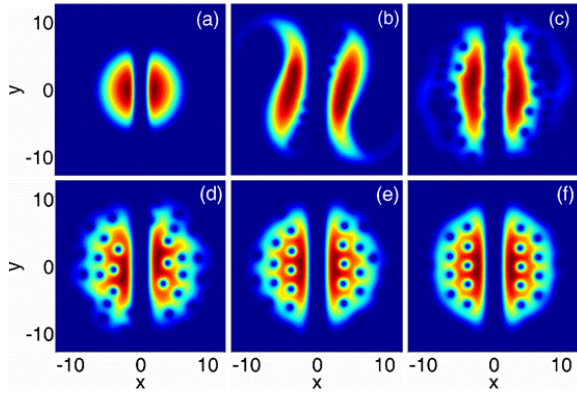


Figure 1 (online color) Time evolution of the density distribution $|\psi|^2$ after the double-well potential with $\lambda = 1$ suddenly begins to rotate with $\Omega = 0.9$, where $c = 600$. The time is (a) $t = 0$, (b) $t = 10$, (c) $t = 50$, (d) $t = 100$, (e) $t = 160$, and (f) $t = 250$. The darker color area indicates the lower density. Here x and y are in units of d_0 , and t is in units of $1/\omega_x$.

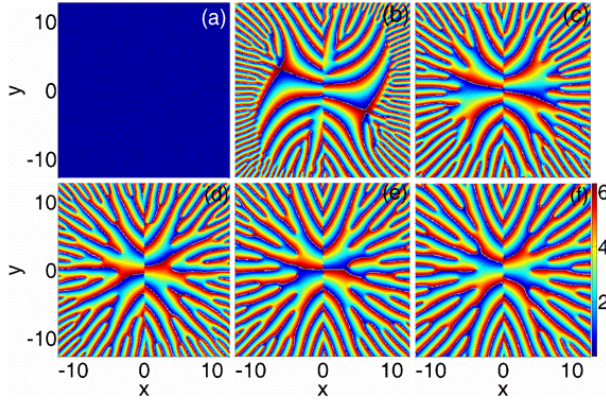


Figure 2 (online color) Time evolution of the phase distribution of $\psi(x, y, t)$ corresponding to that of the density distribution of Fig. 1. The value of the phase varies continuously from 0 to 2π . The darker color area indicates the lower phase.

$\iint \psi^* [-(\nabla_x^2 + \nabla_y^2) + V(x, y) + (c/2)|\psi|^2 - \Omega L_z] \psi dx dy$, respectively. Here $\lambda = 1$, and Ω or c have different values. When $\Omega < 0.59$, we can see that l_z undergoes damped oscillation until a convergent value and ε decreases monotonously to an equilibrium value. When $\Omega \geq 0.59$, however, l_z first experiences damped oscillation, then increases to a new peak value, and finally descends damply to an equilibrium value [see Fig. 3(a)]. At the same time, ε first decreases, then passes over an energy barrier, and finally drops gradually to a convergent value [see Fig. 3(b)]. This distinct difference indicates that the critical rotation frequency for the creation of visible vortices is $\Omega_c = 0.59$ which characterizes the topological phase transition of the rotating DW system. The critical

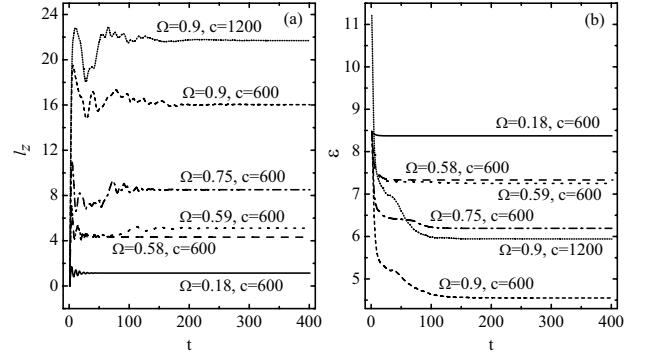


Figure 3 Time evolution of (a) the average angular momentum per atom l_z and (b) the average energy per atom ε for $\lambda = 1$. Here t , l_z and ε are in units of $1/\omega_x$, \hbar and $\hbar\omega_x$, respectively.

frequency $\Omega_c = 0.59$ agrees well with that predicted in Ref. [27]. However, this value is lower than the usual critical frequency $\Omega_{hc} = \sqrt{2}/2 \simeq 0.707$ predicted for a rotating harmonic trap due to the dynamical instability [26, 44]. In view of the even parity of the DW potential, the most probable reason is that here the rotating drive excites mainly the high-order surface mode with $l = 4$ rather than the quadrupole mode with $l = 2$, where $\Omega_{hc} = \sqrt{l}/l$. The small difference between $\Omega_c = 0.59$ and $\Omega_{hc} = 0.5$ is due to the nonlinear interatomic interaction and the presence of the Gaussian barrier as well as the resulting equivalent anisotropy. Moreover, the larger is the Ω (or c) with the same c (or Ω), the larger is the l_z in the equilibrium state and the lower (or higher) is the corresponding ε with a slower (or faster) decline, which reveals that the vortex array is a kind of locally stable quantum state. As shown in Fig. 1 and Fig. 2, with the development of time the hidden vortices and some ghost vortices penetrate toward the areas of high density in the cloud. Due to the DW potential consisting of a harmonic trap and a Gaussian barrier, the vortex formation process is an oscillating dynamical process concerning to the inputting of the external angular momentum, which can explain the oscillation behavior of the angular momentum in Fig. 3(a).

4. Structural change of vortex patterns

The variation of the rotation frequency influences not only the dynamics of the vortex formation but also the equilibrium structure especially the visible vortex pattern of the rotating DW system. In Fig. 4, we display the steady density distributions $|\psi|^2$ at $t = 250$ after the DW potential rotates with different angular frequencies, where $\lambda = 1$ and $c = 600$. The critical rotation frequency at which visible vortices can enter the BEC with $\lambda = 1$ is $\Omega_c = 0.59$ as has been pointed out above and in Ref. [27]. From Fig. 4(a), there is a visible vortex pair for the case of $\Omega = 0.65$,

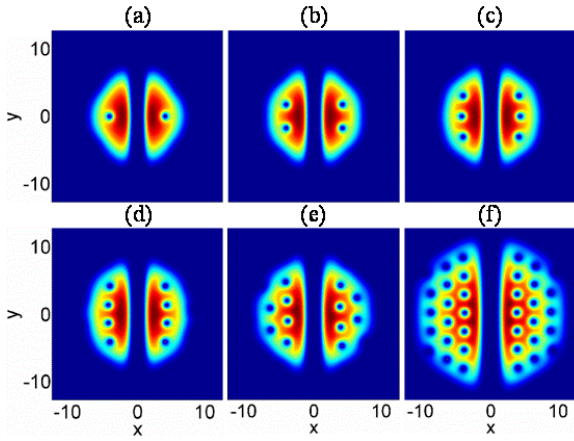


Figure 4 (online color) Steady density distributions $|\psi|^2$ at $t = 250$ for different rotation frequencies: (a) $\Omega = 0.65$; (b) $\Omega = 0.7$; (c) $\Omega = 0.75$; (d) $\Omega = 0.8$; (e) $\Omega = 0.85$; (f) $\Omega = 0.95$. Here $\lambda = 1$ and $c = 600$. The darker color area indicates the lower density.

which is similar to the case of $\Omega = 0.59$ [27]. By comparison, the l_z in the equilibrium state for the former case is larger than that for the latter case (see Fig. 3 in [27]), which is caused by the further approach of the visible vortices to the center of the DW potential and the increase as well as the further concentration of the hidden vortices distributing along the central barrier (the phase profile for $\Omega = 0.65$ is not shown here). With the increase of Ω , the visible vortices enter the BEC with the pair shape and form linear vortex lattice pair as shown in Figs. 4(b)–4(d). When $\Omega = 0.85$, the mirror symmetry is broken and a zigzag vortex lattice pair is formed [see Fig. 4(e)]. Finally, the transition into a triangular vortex lattice pair occurs, which can be seen clearly in Fig. 4(f) and Fig. 1(f). Here a common characteristic is that these visible vortex patterns exhibit the centrosymmetry due to the even parity of the DW potential with respect to the spatial coordinate.

In Fig. 5, we present the steady density distributions $|\psi|^2$ at $t = 250$, where $c = 600$ and λ takes on different values. For the fixed angular frequency $\Omega = 0.9$, when $\lambda = 2$ the visible vortices form a linear lattice pair along the x axis due to the tight confinement in the y -direction of the trap as shown in Fig. 5(a). When $\lambda = 1.5$, the visible vortices become a zigzag vortex lattice pair [see Fig. 5(b)]. A further reduction of λ leads to a formation of a triangular lattice pair of the visible vortices [see Fig. 5(c) and Fig. 1(f)]. The visible vortex patterns for the fixed angular frequency $\Omega = 0.8$ with different values of λ are illustrated in Fig. 4(d) and Figs. 5(d)–(f). With the decrease of λ , the visible vortices entering the BEC by means of vortex pair arrange in a linear lattice pair along the y -direction because of the strong restraint in the x -direction of the trap. In particular, the two halves of the BEC approximate two

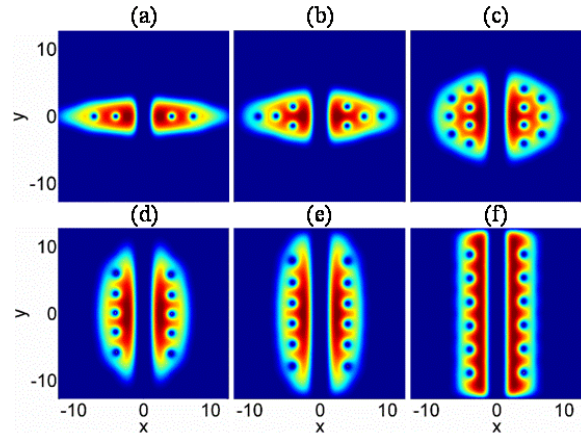


Figure 5 (online color) Steady density distributions $|\psi|^2$ at $t = 250$ for different values of λ , where $c = 600$. (a) $\lambda = 2$, $\Omega = 0.9$, (b) $\lambda = 1.5$, $\Omega = 0.9$, (c) $\lambda = 1.1$, $\Omega = 0.9$, (d) $\lambda = 0.9$, $\Omega = 0.8$, (e) $\lambda = 0.85$, $\Omega = 0.8$, and (f) $\lambda = 0.8$, $\Omega = 0.8$. The darker color area indicates the lower density.

rectangles at $\lambda = 0.8$, where the linear visible vortex lattice pair are similar to two ionic crystals [45].

From Fig. 3(f) in Ref. [27] and Fig. 4(a), we can see that for $0.59 \leq \Omega \leq 0.65$ there are always two visible vortices, i.e., the number of the visible vortices is degenerate with respect to the rotation frequency. Similar degeneracy also occurs in other certain intervals of rotation frequency. In fact, we find that the visible vortex number is possibly degenerate concerning to not only Ω but also λ , for instance, there are all the twelve visible vortices for the cases of $0.8 \leq \lambda \leq 0.85$ with the same $\Omega = 0.8$ as shown in Figs. 5(e)–5(f). The vortex patterns in Fig. 4 and Fig. 5 are rather stable as verified in our simulation. Recently the stability of linear vortex lattice in a rotating anisotropic harmonic trap has been discussed in Ref. [16].

The structure change of vortex patterns in a BEC in a rotating anisotropic harmonic trap has been studied by several theoretical groups [14, 15, 17, 18, 19, 20, 21, 22], where the authors adopted mainly the LLL approximation or Thomas-Fermi (TF) approximation to analyze the vortex structures. However, all of these works did not consider the inevitable dissipation of rotating BECs. In addition, the analytical approaches in Refs. [14, 15, 17, 18, 19, 20, 21, 22] can not be used directly to investigate the steady-state structures of a rotating DW BEC due to the presence of the Gaussian barrier. Here, for the rotating DW BEC there are three different kinds of vortices: visible vortices, hidden vortices and ghost vortices, and each of them have their own unique topological structures [see Fig. 1(f), Fig. 2(f), and Fig. 4], which is very different from the cases of rotating anisotropic harmonic trap. Moreover, as the values of all the parameters are provided above, the structural change of the visible vortex patterns for the rotating DW

BEC with different Ω or different λ is experimentally accessible and examinable.

On the other hand, the linear visible vortex lattice pairs in Fig. 4 and Fig. 5 have potential applications in quantum information as they are somewhat similar to the ionic crystals [45]. For instance, a visible vortex in linear arrangement may be encoded as a quantum bit via a vortex-antivortex superposed state [37, 40, 46, 47, 48]. The flip between the vortex and the antivortex can be realized either by optical methods [49, 50] or by compressing and rehabilitating the trapping potential [48]. The coherence time of vortex quantum bit is long enough to allow a series of operations [16]. In view of the degeneracy of visible vortex number, the small errors of Ω or λ due to experimental uncertainties do not influence the manipulation toward the vortex bits, which is beneficial to the information processing. Another advantage of the linear visible vortex lattices is that each visible vortex has only two nearest neighbors with controllable interaction, where the effect caused by the distant hidden or ghost vortices can be ignored because the particle density in the regions of the potential barrier and the outskirts of the cloud is very small.

5. Conclusion

In summary, we have numerically studied the dynamics of vortex formation and the structure of vortex lattices in a rotating DW BEC by using a phenomenological dissipation model [27]. The vortex formation process in a rotating DW BEC is evidently different from that in a rotating single-well BEC [26]. For the latter case, there are at most two types of vortices: visible vortex and ghost vortex. For our case, there exist three kinds of vortices: visible vortex, ghost vortex and hidden vortex. Once the DW potential rotates, the BEC undergoes complex turbulent oscillation principally consisting of the surface mode with $l = 4$ instead of the usual elliptic oscillation consisting of quadrupole mode with $l = 2$ in a rotating harmonic trap [26]. The hidden vortices and ghost vortices always form earlier than the visible vortices. The critical frequency for the visible vortex generation is marked by a sudden jump in the evolution of the average angular momentum per atom and an inflexion in the evolution of the average energy per atom. The steady vortex patterns of the rotating DW BEC display well centrosymmetry because of the parity effect. It is shown that a structure change of the visible vortex patterns (including the formation of linear and zigzag vortex lattice pairs) can be realized by governing the rotation frequency and the anisotropic parameter of the DW potential. The structural transition of visible vortex patterns makes it possible to artificially manipulate the distribution of vorticity in superfluids and apply the quantized vortices to quantum information processing.

Acknowledgments We thank Biao Wu and Hongwei Xiong for helpful discussions, and thank Yongping

Zhang for valuable suggestions and carefully reading our manuscript. This work is supported by the NSFC (Grants No. 11047033, No. 10965001 and No. 11165009), the International Cooperation Program by Shandong Provincial Education Department, the NSF of Jiangxi Province under Grant No. 2010GQW0033, and the Jiangxi Young Scientists Training Plan under Grant No. 20112BCB23024.

References

- [1] R.J. Donnelly, *Quantum Vortices in Helium II* (Cambridge University Press, Cambridge, 1991).
- [2] D. Vollhardt and P. Wölfle, *The Superfluid Phases of Helium 3* (Taylor & Francis, London, 1990).
- [3] G. Blatter, M.V. Feigelman, V.B. Geshkenbein, A.I. Larkin, and V.M. Vinokur, *Rev. Mod. Phys.* **66**, 1125 (1994).
- [4] P. Bhattacharjee, C.T. Hill, and D.N. Schramm, *Phys. Rev. Lett.* **69**, 567 (1992).
- [5] S. Giorgini, L.P. Pitaevskii, and S. Stringari, *Rev. Mod. Phys.* **80**, 1215 (2008).
- [6] A.L. Fetter, *Rev. Mod. Phys.* **81**, 647 (2009).
- [7] H. Saarikoski, S.M. Reimann, A. Harju, and M. Manninen, *Rev. Mod. Phys.* **82**, 2785 (2010).
- [8] V.I. Yukalov, *Laser Phys. Lett.* **7**, 467 (2010).
- [9] V.I. Yukalov, *Laser Phys. Lett.* **1**, 435 (2004).
- [10] S.K. Adhikari, *Laser Phys. Lett.* **6**, 901 (2009).
- [11] K.W. Madison, F. Chevy, W. Wohlleben, and J. Dalibard, *Phys. Rev. Lett.* **84**, 806 (2000).
- [12] J.R. Abo-Shaeer, C. Raman, J.M. Vogels, and W. Ketterle, *Science* **292**, 476 (2001).
- [13] E. Hodby, G. Hechenblaikner, S.A. Hopkins, O.M. Maragò, and C.J. Foot, *Phys. Rev. Lett.* **88**, 010405 (2002).
- [14] M.Ö. Oktel, *Phys. Rev. A* **69**, 023618 (2004).
- [15] A. Aftalion, X. Blanc, and N. Lerner, *Phys. Rev. A* **79**, 011603(R) (2009).
- [16] S. McEndoo and Th. Busch, *Phys. Rev. A* **82** (2010) 013628.
- [17] S. Sinha and G.V. Shlyapnikov, *Phys. Rev. Lett.* **94**, 150401 (2005).
- [18] S. McEndoo and Th. Busch, *Phys. Rev. A* **79**, 053616 (2009).
- [19] N.Lo Gullo, Th. Busch, and M. Paternostro, *Phys. Rev. A* **83**, 053612 (2011).
- [20] P. Sánchez-Lotero and J. J. Palacios, *Phys. Rev. A* **72**, 043613 (2005).
- [21] A.L. Fetter, *Phys. Rev. A* **75**, 013620 (2007).
- [22] S.I. Matveenko, D. Kovrizhin, S. Ouvry, and G.V. Shlyapnikov, *Phys. Rev. A* **80**, 063621 (2009).
- [23] H. Pu, L.O. Baksmaty, S. Yi, and N.P. Bigelow, *Phys. Rev. Lett.* **94**, 190401 (2005).
- [24] A. Aftalion and I. Danaïla, *Phys. Rev. A* **69**, 033608 (2004).
- [25] C. Ryu, M.F. Andersen, P. Cladé, V. Natarajan, K. Helmer, and W.D. Phillips, *Phys. Rev. Lett.* **99**, 260401 (2007).
- [26] M. Tsubota, K. Kasamatsu, and M. Ueda, *Phys. Rev. A* **65**, 023603 (2002); K. Kasamatsu, M. Tsubota, and M. Ueda, *Phys. Rev. A* **67**, 033610 (2003).
- [27] L.H. Wen, H.W. Xiong, and B. Wu, *Phys. Rev. A* **82**, 053627 (2010).
- [28] R.P. Feynman, *Application of Quantum Mechanics to Liquid Helium*, *Progress in Low Temperature Physics*, Vol. I, edited by C.J. Gorter (North-Holland, Amsterdam, 1955).

- [29] A. Smerzi, S. Fantoni, S. Giovanazzi, and S.R. Shenoy, *Phys. Rev. Lett.* **79**, 4950 (1997).
- [30] Y. Wu and X.X. Yang, *Opt. Lett.* **31**, 519 (2006).
- [31] X.B. Luo, Q.T. Xie, and B. Wu, *Phys. Rev. A* **77**, 053601 (2008).
- [32] D.L. Feder, A.A. Svidzinsky, A.L. Fetter, and C.W. Clark, *Phys. Rev. Lett.* **86**, 564 (2001).
- [33] S. Choi, S.A. Morgan, and K. Burnett, *Phys. Rev. A* **57**, 4057 (1998).
- [34] B. Jackson and E. Zaremba, *Phys. Rev. Lett.* **87**, 100404 (2001).
- [35] C.W. Gardiner, J.R. Anglin, and T.I.A. Fudge, *J. Phys. B* **35**, 1555 (2002).
- [36] C.-H. Hsueh, T.-L. Horng, S.-C. Gou, and W.C. Wu, *Phys. Rev. A* **84**, 023610 (2011).
- [37] L.H. Wen, J.S. Wang, J. Feng, and H.Q. Hu, *J. Phys. B* **41**, 135301 (2008).
- [38] H.W. Xiong and B. Wu, *Laser Phys. Lett.* **8**, 398 (2011).
- [39] B. Wu and Q. Niu, *New J. Phys.* **5**, 104 (2003).
- [40] L.H. Wen, Y.P. Zhang, and J. Feng, *J. Phys. B* **43**, 225302 (2010).
- [41] Y.P. Zhang, L. Mao, and C.W. Zhang, *Phys. Rev. Lett.* **108**, 035302 (2012).
- [42] S. Sinha and Y. Castin, *Phys. Rev. Lett.* **87**, 190402 (2001).
- [43] F. Dalfovo and S. Stringari, *Phys. Rev. A* **63**, 011601 (2001).
- [44] S. Stringari, *Phys. Rev. Lett.* **77**, 2360 (1996).
- [45] G. Birkl, S. Kassner, and H. Walther, *Nature* **357**, 310 (1992).
- [46] K.T. Kapale and J.P. Dowling, *Phys. Rev. Lett.* **95**, 173601 (2005).
- [47] S. Thanvanthri, K.T. Kapale, and J.P. Dowling, *Phys. Rev. A* **77**, 053825 (2008).
- [48] M. Liu, L.H. Wen, H.W. Xiong, and M.S. Zhan, *Phys. Rev. A* **73**, 063620 (2006).
- [49] M.F. Andersen, C. Ryu, P. Cladé, V. Natarajan, A. Vaziri, K. Helmerson, and W.D. Phillips, *Phys. Rev. Lett.* **97**, 170406 (2006).
- [50] K.C. Wright, L.S. Leslie, and N.P. Bigelow, *Phys. Rev. A* **77**, 041601 (2008).